Eur. Phys. J. Plus (2020) 135:818
https://doi.org/10.1140/epjp/s13360-020-00836-4

THE EUROPEAN PHYSICAL JOURNAL PLUS

Regular Article

Sudden contraction effects in nanochannel cross section on the rarefied gas flow characteristics: LBM analysis

Ehsan Kamali Ahangar, Javad Abolfazli Esfahani[a], Mohammad Bagher Ayani

Department of Mechanical Engineering, Ferdowsi University of Mashhad, Mashhad 91775-1111, Iran

Received: 2 September 2020 / Accepted: 5 October 2020 / Published online: 13 October 2020

Abstract This mesoscopic investigation aims to study the rarefied gas flow inside a contracting nanochannel in the slip and transitional regimes by two relaxation time lattice Boltzmann method. Bosanquet-type effective viscosity and distribution functions correction at the corner points are used to enhance the precision of slippage velocity on the walls. The boundary conditions at the entrance and exit sections of the nanochannel are assumed nonequilibrium-equilibrium distribution functions. The bounce back-specular reflection boundary conditions are considered for the wall exteriors. It is found that both momentum and rarefaction play essential roles concerning the separation phenomena in nanochannel flow. The higher outlet Knudsen number possesses the higher effective viscosity and shear stress, while the vortices become smaller and tend to disappear at higher Knudsen numbers. The results of the direct simulation Monte Carlo method have been utilized to validate the present numerical prediction, and an outstanding agreement between the results is shown.

1 Introduction

One of the significant applications of rarefied gas flow is in the microfluidic-nanofluidic devices. Due to different operations of rarefied gas flows, the rarefaction characteristic is an important issue, and the Knudsen number shows it. The gaseous stream is apportioned into four customary regimes based on the Knudsen number including continuous regime ($Kn < 0.001$), slip regime ($0.001 < Kn < 0.1$), transition regime ($0.1 < Kn < 10$), and free molecular regime ($Kn > 10$) [1, 2]. Most pioneering research has focused on simulations of micro-nano channels with uniform cross-sections. Researchers have simulated the impact of surface harshness for gaseous flow inside the microchannel using different methods. These included molecular dynamics [3], molecular dynamics-continuum hybrid method for micro/nanoscale flow with constant wall temperatures [4], diluted microscale flow using mesoscopic scheme [5], and analytical solutions for gas stream in the microchannel at a broad range of Knudsen numbers [6]. The lattice Boltzmann method (LBM) is successful in rarefied gas dynamics because of its ability to simulate complex geometries with low computational cost in comparison to the other existing methods such as direct simulation Monte Carlo (DSMC).

Arkilic et al. [7] used perturbation expansion of the Navier–Stokes equations with a first-order adjustment to the velocity slippage. They forecast the mass flow rate in the slip regime

[a] e-mail: abolfazl@um.ac.ir (corresponding author)

inside the microchannel, thoroughly. Ho et al. [8] surveyed the separation phenomena in the bent microchannel employing kinetic equation. Two types of vortexes are discussed based on rarefaction parameter. By Kn number rises, the recirculation length diminishes. Using a finite volume method namely simplified discrete unified gas kinetic scheme, Zhong et al. [9] examined the incompressible flow in all regimes. Baranger et al. [10] proposed a BGK model for simulating the thermal rarefied flow which considers the nonequilibrium interactions in rarefied flow. They did this study by utilizing the Chapman–Enskog theory and Navier–Stokes equations. Wu and Struchtrup [11] evaluated and developed the various boundary conditions (BCs) of the gas kinetic including Maxwell, Cercignani–Lampis, and Epstein. They solved the linearized Boltzmann equation for capturing the gas-surface interactions. Taguchi et al. [12] simulated the rarefied flow at the vicinity of rotational sphere based on the linearized Boltzmann equation. Velocity and heat quantities were derived by diverging parameters that were linked to jump discontinuity. In the slip regime, Varade et al. [13] investigated the rarefied flow through the tube with sudden expansion experimentally. They found that the moving forward of the fluid flow lead to shear stress increase at the wall surface and rising in pressure drop in comparison with regular shape tube. Meolans et al. [14] investigated gaseous flow through the convergent-divergent microchannel using theoretical and experimental methods. They stated that the pressure reduction is significantly higher on the divergent side of the channel. They mentioned that this difference somehow disappears with the flow tendency toward each of the continuous and free molecular regime. The analytical method was based on the slip velocity boundary condition. Analytical methods can mimic the diluted microscale gaseous flow in simple geometries and can not investigate the behavior of fluid flow in complex geometries. Therefore, previous researchers used a DSMC for simulating gaseous flow in micro/nanoscales.

Taassob et al. [15] investigated a rarefied gas stream in a bend microchannel using the DSMC scheme. They found that increasing the radius of the corner indicates a higher mass flow rate. They also implemented a curvature instead of a sharp bend leads to increased average shear stress and velocity slip. Gavasane et al. [16] modeled diluted microscale gaseous flow using the DSMC method in a microchannel with a backward-facing step in both slip and transitional regimes. They considered a higher Reynolds number for the slip regime in comparison to the transition one to demonstrate the impact of Reynolds number on the obtained Mach values. Their results show that the Mach value in the slip regime is greater than that of the transition regime, and the separation length is shorter in the cases of flow tendency to the transition regime or increased Knudsen number. Sazhin [17] probed the rarefied gas flow inside the channel with irregular cross -section by the DSMC approach. He reported the relationship between rarefaction parameter (δ) and nondimensional mass flow rate (Q^*). As the main findings of his research, the δ parameter changes from 0 to 1000 and found a direct correlation with Q^* for both aspect ratios of 1 and 10. Nabapure et al. [18] studied the rarefied gas flow in the forward-facing step by DSMC method at a vast range of Kn numbers (slip to free molecular regimes). They found that the normalized gas characteristics increase, while the Kn number rises. The separation phenomenon has occurred at the range of $Kn < 10$, however, it disappeared at the $Kn > 10$. Previous Pioneers used a robust and reliable method (LBM) to simulate the rarefied gas flows because of less running time in comparison with the complicated and challenging DSMC method. A lot of LBM applications relative to fluid flow and heat transfer were found in varying numerical simulations [19–28]. Tucny et al. [29] carried out a comparison study between existing and extended BCs in rarefied gas flow by using the LBM. A model BC by the combination of bounce back and diffusive reflection is suggested which captured the effective viscosity accurately.

Timokhin and Tikhonov [30] simulated the microscale gas flow inside the microchannel, including two solid objects by the single relaxation time-LBM. They reported that the vortexes were generated in the vicinity of the solid object due to a negative pressure gradient. Niu et al. [31] carried out the simulation process for microscale flow over the airfoil with a low Reynolds number by using one relaxation time of the LBM approach. It is found that flow with a higher Reynolds number has a lower pressure coefficient, and the pressure coefficient trend declines along with the geometry (x-direction). Wang et al. [32] used LBM for gas-particle flow simulation at the mesoscopic scale over a backward-facing step. They successfully captured the various separation lengths at high Reynolds numbers in the transitional regime. It is also found that the lattice Boltzmann-cellular automata (LB-CA) are capable of capturing the average and fluctuating velocities. Li et al. [33] generalized the Boltzmann equation and showed that the accuracy of the results was affected by the existing force term, an outcome of acceleration, in the flow. They solved the microscale gaseous stream implementing multiple relaxation times. They noticed the substantial error in deviation of pressure values from the linear ones compared to the DSMC results. By using a 3-dimensional LB model for fluid flow, Kakouei et al. [34] investigated the behavior of the flow in different porous structures. They observed that the pressure gradient increases as velocity increases and also reported, there is an inverse relationship between apparent permeability and Reynolds number.

Ho et al. [35] surveyed penetration of rarefied gas in a porous media in 2D using LBM with the multiple relaxation times (MRT) collision model. They reported that the penetration rate is increased with the dilution and is independent of the geometry. They analyzed the accuracy of used wall functions in the velocity and temperature profiles for the transitional regime. They claimed that the results of the higher-order LBM could increase the exactness of velocity and temperature distributions for Fourier and shear-driven flows for Knudsen numbers less than 5. Wang et al. [36] modeled the diluted gaseous stream in the porous media using the MRT-LBM. They reported that the penetration rate is considerably influenced by the pressure and is increased with increasing porosity. Wang et al. [37] presented a review paper on the use of the LBM intended for the gas flow in a microscale with a constant temperature. They provided the collision operator using MRT, two relaxation times (TRT), and the various slip boundary conditions like bounce back, specular reflection, Maxwellian diffuse reflection, combined form, and Langmuir slip boundary. They suggested two approaches for the effect of the Knudsen layer on the slippage velocity: effective viscosity and high order LBM.

Norouzi and Esfahani [38] implemented a model with TRT due to less running time and simplicity in computer coding compared to the MRT-LBM. They enhanced the slip velocity by anti-symmetrical relaxation time. Neglecting the impacts of the Knudsen layer was the weakness of their research. The diluted gas microflow is modeled in the backward-facing microstep [39] and irregular shape microchannel with multiple throats [5] by the TRT-LBM method in both slip and transition regimes. They investigated the effects of several parameters, such as pressure, velocity, and mass flow rate on the flow pattern. They utilized Zou-He boundary conditions for inlet–outlet of the mentioned geometry, and also illustrated the influence of Knudsen number on vortices. They considered an analytical Power-law function that captures the impacts of the Knudsen layer in the transition regime. They separately adopted specific slip coefficients for each regime by trial and error. As the weaknesses of their work, they did not base on kinetic theory and did not consider the distribution function correction at the corner points.

The goal of the present study is to survey the contraction effect on rarefied gas flow characteristics inside the nanochannel by applying particular symmetric relaxation time for each slip and transition regime. Besides, manipulating the TRT model with finding anti-symmetrical relaxation time and r parameter using bounce back-specular reflection (BSR) boundary con-

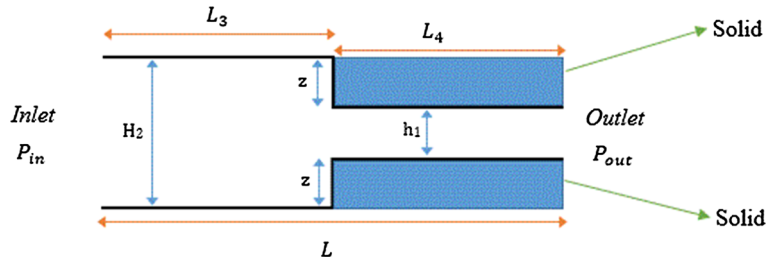

Fig. 1 The schematic view of the contracting nanochannel

ditions is the innovation of the current research. The precision of the results is enhanced by using the TRT model based on viscosity correction, anti-symmetric relaxation time in the transition regime, and consideration of the nonequilibrium-equilibrium distribution functions for input–output of the nanochannel. The outcomes of the current LBM simulation come up with an excellent agreement with the DSMC results that represent the TRT model accuracy.

2 Lattice Boltzmann method

In this section, the TRT modeling of the lattice Boltzmann, necessity for the current work, is briefly reviewed.

2.1 Physical model

Figure 1 demonstrates a contracting nanochannel with an aspect ratio of 19 to 1. H_2 is the nanochannel height, and L is the total length. L_3 and H_2 are the nanochannel length and height of the channel before contraction, respectively. Furthermore, L_4 and h_1 are the nanochannel length and height after the contraction, respectively, and z indicates the contraction value from both sides of the nanochannel. The pressure ratio is presented by $\Pi = \frac{P_{\text{in}}}{P_{\text{out}}}$ and is equal to 1.005. The outlet values of Knudsen numbers have been employed to simulate gas flow in the slip and transition regimes. The inlet and outlet densities of the gas stream are considered as $\rho_{\text{in}} = 1.005\left(\frac{\text{mu}}{(\text{lu})^3}\right)$ and $\rho_{\text{out}} = 1\left(\frac{\text{mu}}{(\text{lu})^3}\right)$, respectively. The speed of sound is applied to nondimensional velocities.

The parameters that appear in Fig. 1 are as follows:

$$L_3 = L_4 = \frac{L}{2}, h_1 = z = \frac{H_2}{3}, \alpha = \frac{H_2}{h_1}$$

where α is the shrinkage coefficient and considered as 3 in the simulation.

2.2 Governing equations

In current decades, a model with MRT solver is utilized, but for improving the computational cost, Norouzi and Esfahani [38] have employed a two relaxation times model, which are suitable in rarefied gas flow simulation in a micro-nano channel with satisfactory precision. The standard form of the mesoscopic approach with TRT solver is as follows:

$$f_i(\boldsymbol{x} + \boldsymbol{c}_i \delta t, t + \delta t) - f_i(\boldsymbol{x}, t) = \Omega(f_i) \tag{1}$$

where $f_i(\boldsymbol{x}, t)$, Ω, and $\boldsymbol{c}_i$ are the local distribution function for the specific location and time, collision operator, and discrete velocity in any route, respectively. Besides, the *D2Q9* network with $\delta t = 1$ (time step) is selected for the simulation.

The collision step is formed by two symmetric and anti-symmetric sections, and the relation between them was presented by Ginzburg [40] as:

$$\Omega(f_i) = -\tau_s^{-1}\left(f_i^s(\boldsymbol{x}, t) - f_i^{seq}(\boldsymbol{x}, t)\right)_s - \tau_a^{-1}\left(f_i^a(\boldsymbol{x}, t) - f_i^{aeq}(\boldsymbol{x}, t)\right)_a \tag{2}$$

where subscripts of s and a are denoted for the symmetric and asymmetric issues.

The equilibrium distribution function can be introduced by [38]:

$$f_i^{eq} = \omega_i \rho\left[1 + \frac{\boldsymbol{c}_s \cdot \boldsymbol{V}}{RT} + \frac{(\boldsymbol{c}_s \cdot \boldsymbol{V})^2}{2(RT)^2} - \frac{\boldsymbol{V}^2}{2RT}\right], RT = \frac{1}{3} \tag{3}$$

where $c_s = \frac{c}{\sqrt{3}}$ is the speed of sound, $c = \delta x/\delta t$. δx is the space step and $\delta x = \delta y = 1$.

The local symmetric and asymmetric distribution functions for the *D2Q9* network were introduced by Ginzburg [40] corresponding to the following equation:

$$f_i^s = \frac{1}{2}(f_i - f_{-i}),\ f_i^a = \frac{1}{2}(f_i - f_{-i}) \tag{4}$$

$$f_i^{\text{seq}} = \frac{1}{2}\left(f_i^{\text{eq}} + f_{-i}^{\text{eq}}\right),\ f_i^{\text{aeq}} = \frac{1}{2}\left(f_i^{\text{eq}} - f_{-i}^{\text{eq}}\right) \tag{5}$$

The discrete velocities in each direction and the weight factors for the particles of the lattice network are labeled as follows [33]:

$$\boldsymbol{c_i} = \begin{cases} (0,0) & i = 0 \\ \left(\cos\left[\frac{(i-1)\pi}{2}\right], \sin\left[\frac{(i-1)\pi}{2}\right]\right)c & i = 1, 2, 3, 4 \cdot \\ \left(\cos\left[\frac{(2i-9)\pi}{4}\right], \sin\left[\frac{(2i-9)\pi}{4}\right]\right)\sqrt{2c}\ i & = 5, 6, 7, 8 \end{cases} \tag{6}$$

$$\omega_0 = \frac{4}{9}, \omega_{1-4} = \frac{1}{9}, \omega_{5-8} = \frac{1}{36} \tag{7}$$

The properties of density, velocity, and pressure in a macroscopic state using the LBM can be network are labeled as follows [33]:

$$\rho = \sum_{i=0}^{8} f_i, \boldsymbol{V} = \frac{1}{\rho}\sum_{i=0}^{8} f_i \boldsymbol{c_i}, P = \rho c_s^2 \tag{8}$$

2.3 Effective viscosity and relaxation times

Based on the kinetic theory of gases, molecular free path λ is a function of dynamic viscosity μ, pressure P, temperature T, and gas constant (R), and is defined as follows [33]:

$$\lambda = \frac{\mu}{P}\sqrt{\frac{\pi RT}{2}} \tag{9}$$

In the above relation, the pressure for an ideal gas is $P = \rho RT$.

Based on the Chapman–Enskog analysis [41], gas viscosity is defined as follows:

$$\mu = 1.016 \times \frac{5}{16}\frac{m}{d^2}\sqrt{\frac{RT}{\pi}} \approx 0.5\rho\bar{c}\lambda \tag{10}$$

where m, d, and $\bar{c} = \sqrt{\frac{8RT}{\pi}}$ are molecular mass, molecular diameter, and mean molecular velocity, respectively. This velocity is valid for an unlimited gas stream. In the case of the

unbounded gas flow system, the movement way of some gas molecules turns out to be tinier, which is due to the collision among gas molecules and solid walls. This collision is neglected in comparison with intermolecular collisions when Kn$\ll 1$.

According to Eq. 10, viscosity is defined as $\mu_0 = a_0\rho\bar{c}\lambda$ where $a_0 = 0.5$. In the slip regime, μ_0 is effective viscosity. However, for gas streams with high Knudsen numbers in the transition regime, intermolecular collisions meaningfully decrease because of an increase in rarefaction effects. For free molecular flows (with Kn$\gg 1$), the only collision between molecules and walls should be measured [42]. Therefore, the viscosity should be defined using the characteristic length (H) as $\mu_\infty = a_\infty\rho\bar{c}H$ in the free molecular flow regime, where a_∞ is a numerical constant when λ is large enough [43]. The Bosanquet-type effective viscosity can be achieved for rarefied gas flows with a finite Knudsen number [43].

$$\frac{1}{\mu_e} = \frac{1}{\mu_0} + \frac{1}{\mu_\infty} \tag{11}$$

where μ_e, μ_0 and μ_∞ are an effective viscosity for the flow in transition regime, a viscosity in the slip flow regime, and a viscosity for the free molecular flow regime, respectively. Rearranging the Eq. (11), the effective viscosity in the transition regime is obtained as $\mu_e = \frac{\mu_0}{(1+aKn)} = \frac{a_0\rho\bar{c}\lambda}{(1+aKn)}$ where rarefaction effect (a) is calculated as $a = \frac{a_0}{a_\infty}$. This coefficient has been considered as 2.2 by Beskok et al. [42] for flow in a channel. Yuhong and Chan [44] later selected the value of 2 for this coefficient. Therefore, the amount of $a = 2$ is designated in the current transition regime simulation.

The amount of symmetrical relaxation time is correlated to the Knudsen number that was introduced by Liu and Guo [45], and is applied for simulation in the slip regime as follows:

$$\tau_s = 0.5 + \sqrt{\frac{6}{\pi}}\frac{\mathrm{Kn}\cdot H}{\delta x} \tag{12}$$

But Li et al. [46] used the following relation for the symmetrical relaxation time in the transition regime:

$$\tau_s = 0.5 + \sqrt{\frac{\pi}{6}}\frac{\mathrm{Kn}\cdot H}{\delta x(1+a\mathrm{Kn})},\ a = 2 \tag{13}$$

where Kn and H denoted Knudsen number and the local height of contracting nanochannel, respectively. The symmetric relaxation time (τ_s) is founded by the viscosity in the computational domain.

2.4 Boundary conditions

In rarefaction gas flow with constant temperature, Guo et al. [47] provided the following second-order relation for the slip velocity:

$$u^{\mathrm{slip}} = A_1\sigma\lambda\left.\frac{\partial u}{\partial y}\right|_{\mathrm{Wall}} - A_2\lambda^2\left.\frac{\partial_u^2}{\partial y^2}\right|_{\mathrm{Wall}} \tag{14}$$

where A_1 and A_2 are slip coefficients. Various researchers suggest various values for these coefficients; e.g., $A_1 = 1.1466$ and $A_2 = 0.9756$ by Cercignani et al. [48], $A_1 = 1.11$ and $A_2 = 0.61$ by Hadjiconstantinou [49], and $A_1 = 1$ and $A_2 = 0.5$ by Hsia [50]. Loyalka et al. [51, 52] represented a correction of Maxwell's assert using the approximation technique in kinetic theory. Moreover, Loyalka et al. [51, 52] and Guo et al. [47] proposed A_1 one of the slip coefficients that is equal to $(1 - 0.1817\sigma)$. Li et al. [33] were able to adjust their results with the results of the solution of linear Boltzmann equations by considering the coefficient as $A_2 = 0.8$.

In this study, A_1 and A_2 coefficients have been used as $A_1 = \left(\frac{2-\sigma}{\sigma}\right)(1 - 0.1817\sigma)$ and $A_2 = 0.8$ in both flow regimes where $\sigma = 1$ is the tangential momentum accommodation coefficient (TMAC). As mention before, the pressure at the input and output segments of the nanochannel is fixed as the boundary conditions, so that the pressure ratio of $\Pi = \frac{P_{\text{in}}}{P_{\text{out}}} = 1.005$ is considered for this work. The inlet and outlet boundary conditions are nonequilibrium-equilibrium distribution functions and are defined by the following relation [53].

After the streaming, distribution functions f_2, f_3, f_4, f_6, and f_7 are obtained, and the following relation is established between $u_{(0,j)}$ and f_1, f_5, f_8:

$$f_1 + f_5 + f_8 = \rho_{in} - (f_0 + f_2 + f_3 + f_4 + f_6 + f_7) \tag{15}$$

$$f_1 + f_5 + f_8 = \rho_{in} u_{(0,j)} + (f_3 + f_6 + f_7) \tag{16}$$

$$f_5 - f_8 = -f_2 + f_4 - f_6 + f_7 \tag{17}$$

$u_{(0,j)}$ is derived from Eqs. 15 and 16 as:

$$u(0, j) = 1 - \left(\frac{f_0 + f_2 + f_4 + 2(f_3 + f_6 + f_7)}{\rho_{\text{in}}}\right) \tag{18}$$

$$f_1 = f_3 + \frac{2}{3}\rho_{\text{in}} u(0, j) \tag{19}$$

$$f_5 = f_7 + \left(f_5^{\text{eq}} - f_7^{\text{eq}}\right) \tag{20}$$

$$f_8 = f_6 + \left(f_8^{\text{eq}} - f_6^{\text{eq}}\right) \tag{21}$$

where ρ_{in} in the above equation is calculated from the inlet pressure. To calculate the outlet velocity, the following relations are used:

$$u(n, j) = -1 + \left(\frac{f_0 + f_2 + f_4 + 2(f_1 + f_5 + f_8)}{\rho_{\text{out}}}\right) \tag{22}$$

$$f_3 = f_1 - \frac{2}{3}\rho_{\text{out}} u(n, j) \tag{23}$$

$$f_6 = f_7 + \left(f_6^{\text{eq}} - f_7^{\text{eq}}\right) \tag{24}$$

$$f_7 = f_6 + \left(f_7^{\text{eq}} - f_6^{\text{eq}}\right) \tag{25}$$

where ρ_{out} in the above equation is obtained from the outlet pressure.

The amount of Knudsen number in each cross-section, for the isothermal flow in a contractive nanochannel, is determined by using the following equation:

$$Kn_{\text{out}}.H_{\text{out}}.P_{\text{out}} = \text{Kn}(x) \cdot H(x) \cdot P(x) \rightarrow \text{Kn}(x) = \frac{\text{Kn}_{\text{out}} \cdot H_{\text{out}} \cdot P_{\text{out}}}{H(x) \cdot P(x)} \tag{26}$$

This dependency of Kn is vital in solving the problem because of the decrease in lateral cross section [46].

In the simulation of the mentioned geometry, the BSR boundary conditions are considered for the walls. The use of these boundary conditions results in more accurate results for micro-nanochannels with a variable cross-section. The boundary conditions for the lower wall before and after contraction are as follows [53]:

$$f_2 = f_4 \tag{27}$$

$$f_6 = r f_8 + (1 - r) f_7 \tag{28}$$

$$f_5 = r f_7 + (1 - r) f_8 \tag{29}$$

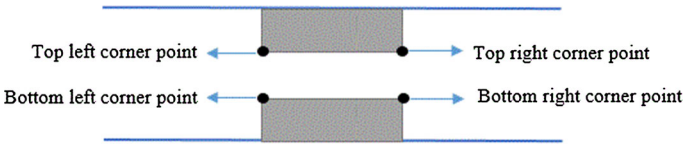

Fig. 2 Nanochannel with solid objects

For the upper wall before and after contraction, they are listed as:

$$f_4 = f_2 \tag{30}$$

$$f_7 = rf_5 + (1-r)f_6 \tag{31}$$

$$f_8 = rf_6 + (1-r)f_5 \tag{32}$$

Lastly, for the vertical walls, they are listed as:

$$f_3 = f_1 \tag{33}$$

$$f_6 = rf_8 + (1-r)f_5 \tag{34}$$

$$f_7 = rf_5 + (1-r)f_8 \tag{35}$$

It is necessary to correct distribution functions at the corner points due to the intersection of the two surfaces in the LBM simulation. If the solid object is defined as the Fig. 2 for the nanochannel, corner points correction based on a distribution function and BSR boundary conditions is derived as follows [54]:

Top left corner point:

$$f_3 = f_1 \tag{36}$$

$$f_4 = f_2 \tag{37}$$

$$f_6 = rf_8 + 0.5 \times (1-r)f_5 + 0.5 \times (1-r)f_7 \tag{38}$$

$$f_7 = rf_5 + 0.5 \times (1-r)f_8 + 0.5 \times (1-r)f_6 \tag{39}$$

$$f_8 = rf_6 + 0.5 \times (1-r)f_5 + 0.5 \times (1-r)f_7 \tag{40}$$

Top right corner point:

$$f_1 = f_3 \tag{41}$$

$$f_4 = f_2 \tag{42}$$

$$f_5 = rf_7 + 0.5 \times (1-r)f_6 + 0.5 \times (1-r)f_8 \tag{43}$$

$$f_8 = rf_6 + 0.5 \times (1-r)f_5 + 0.5 \times (1-r)f_7 \tag{44}$$

$$f_7 = rf_5 + 0.5 \times (1-r)f_6 + 0.5 \times (1-r)f_8 \tag{45}$$

Bottom left corner point:

$$f_2 = f_4 \tag{46}$$

$$f_3 = f_1 \tag{47}$$

$$f_7 = rf_5 + 0.5 \times (1-r) f_6 + 0.5 \times (1-r) f_8 \tag{48}$$

$$f_6 = rf_8 + 0.5 \times (1-r) f_7 + 0.5 \times (1-r) f_5 \tag{49}$$

$$f_5 = rf_7 + 0.5 \times (1-r) f_6 + 0.5 \times (1-r) f_8 \tag{50}$$

Bottom right corner point:

$$f_2 = f_4 \tag{51}$$

$$f_1 = f_3 \tag{52}$$

$$f_6 = rf_8 + 0.5 \times (1-r) f_5 + 0.5 \times (1-r) f_7 \tag{53}$$

$$f_5 = rf_7 + 0.5 \times (1-r) f_6 + 0.5 \times (1-r) f_8 \tag{54}$$

$$f_8 = rf_6 + 0.5 \times (1-r) f_5 + 0.5 \times (1-r) f_7 \tag{55}$$

In the above equations, r is a momentous parameter in connection with the obtained results because the slip velocity on the wall is linked to A_1 coefficient. Hence, Li et al. [33] introduced a relationship for A_1 and anti-symmetrical relaxation time (τ_a) and Guo et al. [55] provided the slip velocity relation (u^{slip}) for the smooth wall by considering BSR boundary conditions:

$$u^{\text{slip}} = \frac{4}{(1-r)} r\sqrt{6/\pi}\,\text{Kn} + \frac{2}{\tau_{\text{sa}}}\pi(\tau_s - 0.5)^2 \text{K}n^2 \tag{56}$$

where $\tau_{\text{sa}} = 16(\tau_s - 0.5)(\tau_a - 0.5)$, and the analytical solution for the second-order slip velocity concerning boundary conditions is obtained as follows:

$$u^{\text{slip}} = 4A_1\text{Kn} + 8A_2\text{Kn}^2 \tag{57}$$

With equalizing both Relations 56 and 57, the following equations are obtained for r and τ_a based on slip boundary:

$$r = \left[1/\left(1 + \sqrt{\pi/6}A_1\right)\right] \tag{58}$$

$$\tau_a = \left[\left(\pi A_2(2\tau_s - 1)^2 + 3\right)/(8(2\tau_s - 1))\right] + 0.5 \tag{59}$$

3 Results and discussion

3.1 Grid independency

The flow in the nanochannel is considered for three grid sizes including 400×22, 799×43, and 1597×85 in slip regime ($\text{Kn}_o = 0.05$). A point at $\left(\frac{X}{L}, \frac{Y}{H}\right) = (0.2, 0.5)$ in the domain is selected. It is observed that, at this point, nondimensional velocity values for both 799×43 and 1597×85 grid sizes are close. Therefore, grid size 799×43 is selected to deduct computational costs (Table 1).

Table 1 The centerline velocity of the nanochannel for different Grid numbers

Grid size		
400×22	799×43	1597×85
Velocity at $\left(\frac{X}{L'}\frac{Y}{H}\right) \times 10^{-4} = (0.2, 0.5)$		
2.33	2.17	2.13
Error (%)		
7.37	1.88	

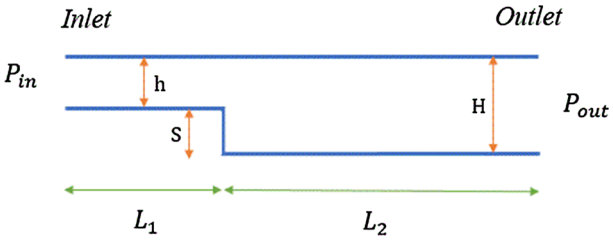

Fig. 3 Two-dimensional microchannel with a backward-facing microstep

3.2 Results analysis

For comparison the present model with previous researchers' methodology, a microchannel with backward-facing microstep with the aspect ratio of 10 to 1 for each section is used, see Fig. 3. In the figure, H, L_1, and L_2 are equal to 1 μm, 5 μm, and 10 μm, respectively, and h and s are both the same to 0.5 μm. The pressure ratio of $\Pi = \frac{P_{\text{in}}}{P_{\text{out}}} = 5$, and the inlet Reynolds numbers for slip and transition regimes at 6.43 and 0.052, respectively, are used [16].

Figures 4a, b are the pressure plots on the upper wall ($Y^* = \frac{y}{H} = 1$) and centerline ($Y^* = \frac{y}{H} = 0.5$) in the slip (Kn= 0.0311) and transition regimes (Kn = 1.3247), respectively. As observed in Fig. 4a, owing to the presence of backward-facing microstep at $X^* = 1/3$ that leads to cross-section decline and Kn number rise, the pressure profile is detected with a decline tend. At the junction in Fig. 4b, the same trend is perceived; however, the declining amplitude is larger than that of in Fig. 4a. Figures 4c, d show the Mach numbers of the entrance center ($Y^* = \frac{y}{H} = 0.75$), the center of the vertical wall ($Y^* = \frac{y}{H} = 0.25$), and the bottom wall ($Y^* = \frac{y}{H} = 0$) in the microchannel for both regimes. It can be seen in Fig. 4c, there is an increase-reduction pulse in Mach number due to velocity (in lattice unit) change. By analyzing the velocity quantities and finding a maximum value at the microchannel outlet on account of Kn number growth, the Mach numbers have a rising pulse at $Y^* = 0$ and $Y^* = 0.25$. All of the plots indicate an acceptable agreement between LBM and DSMC [16] results. Figure 4e demonstrates the nondimensional velocity, relative to its mean value, along the y-direction at Knudsen number of 1.13. Based on the velocity values of the DSMC approach in Fig. 4e, it can be seen, the obtained slippage and centerline velocities by the present scheme is more accurate compared to the calculated velocity values by our previous research [5] due to considering the distribution functions corrections at the corner point and nonequilibrium-equilibrium distribution functions as boundary conditions at inlet–outlet geometry. In all plots, the pressure ratio is fixed at 5.

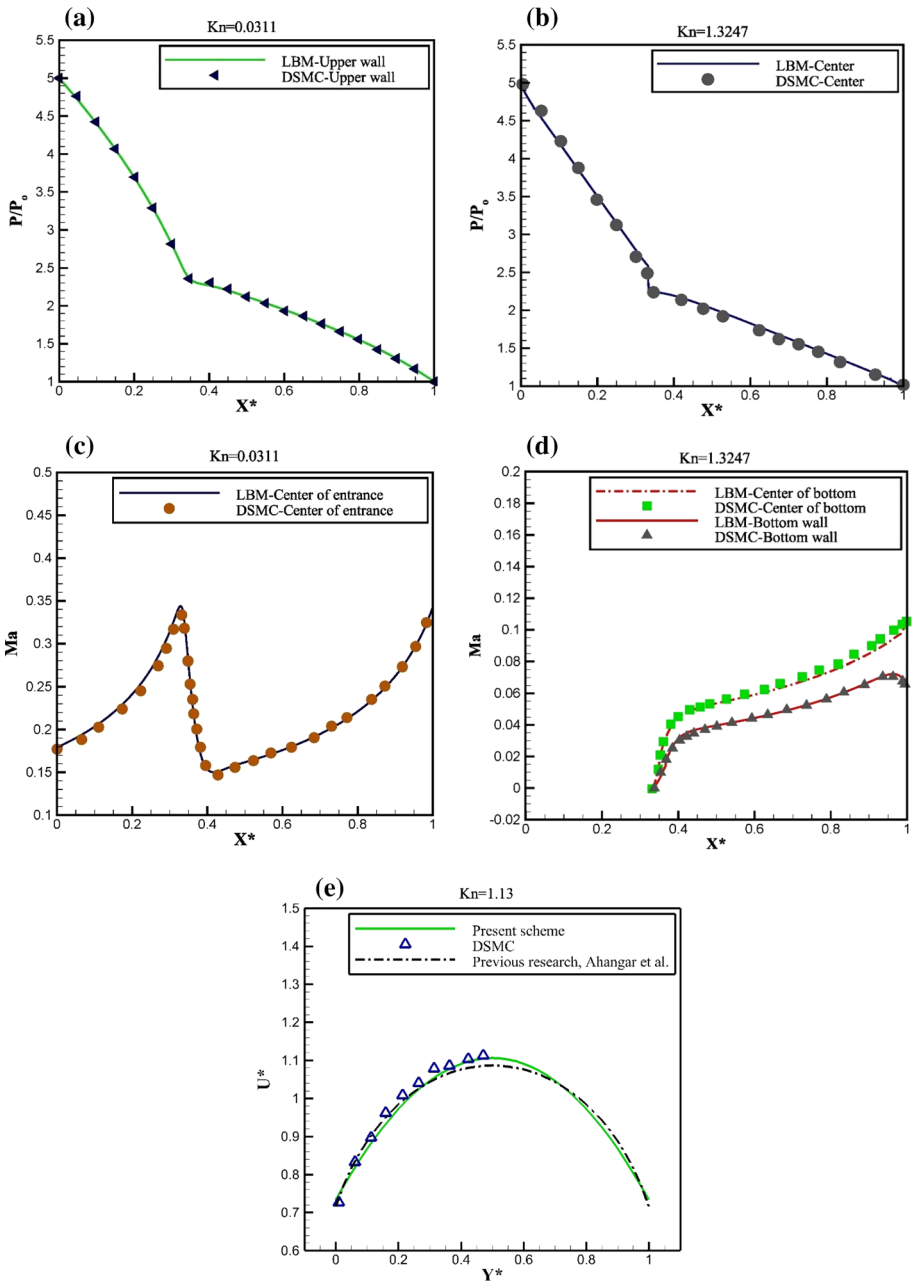

Fig. 4 Results comparison between the present model with DSMC [16] including **a** dimensional pressure of top wall at Kn= 0.0311, **b** centerline pressure at Kn= 1.3247, **c** Mach number of entrance center in slip regime, **d** Mach number at $Y^* = (0 \text{ and } 0.25)$ in transition regime, and **e** comparison of dimensionless velocity between DSMC [16], our previous study [5], and present LBM at Kn= 1.13

Figure 5 demonstrates the variation of nondimensional pressure in both slip and transition regimes, at the centerline and the center of the bottom vertical wall in the nanochannel. Figure 5a displays the centerline pressure for various outlet Knudsen numbers along the

nanochannel length. This figure shows a rapid reduction of the centerline pressure at the nanochannel contraction, $X^* = 0.5$. Due to higher pressure at the inlet of nanochannel, the plot has a downward trend. Moreover, the flow has lower nondimensional pressure for elevated outlet Knudsen number. The amplitude of pressure alterations before the junction is less than that of after contraction owing to smaller Kn number change from $X^* = 0$ to $X^* = 0.5$ compared to after the junction. Figure 5b shows the variation of pressure in the middle of the bottom vertical wall ($Y^* = \frac{Y}{H_2} = 0.167$) is parabolic. At the slip regime, the pressure decreases along the channel before reaching $X^* = 0.48$, and is equal to 1.004826 and 1.004813 for Kn= 0.0095 and 0.08, respectively. The pressure increases past $X^* = 0.48$. Besides, the flow with lower Knudsen numbers leads to higher nondimensional pressure in the middle of the bottom vertical wall. Similar behavior is detected in the transition regime from the inlet of the channel up to $X^* = 0.48$, shown in Fig. 5c. While rarefied flow moves into the nanochannel, the pressure gradient tends to be favorable. However, in both Fig. 5b, c, an adverse pressure gradient is identified near the sudden contraction due to vortex generation. Figure 6 indicates the pressure and density contours in both slip and transitional regimes. Figure 6a reveals the pressure contour in the slip regime, $\mathrm{Kn}_o = 0.0095$. Based on the equation of $\rho = 3P$, the pressures at the input and output of nanochannel are 0.335 ($\frac{\mathrm{mu}}{\mathrm{lu}\cdot(\mathrm{tu})^2}$) and 0.333 ($\frac{\mathrm{mu}}{\mathrm{lu}\cdot(\mathrm{tu})^2}$), respectively. Figure 6b displays the density contour in the transition regime ($\mathrm{Kn}_o = 1.3$). The density value at the inlet and outlet of the nanochannel is equal to 1.005 ($\frac{\mathrm{mu}}{(\mathrm{lu})^3}$) and 1 ($\frac{\mathrm{mu}}{(\mathrm{lu})^3}$), respectively. Both 6a and 6b contours change linearly, and the pressure and density values decrease from the nanochannel inlet toward the outlet. It is noted that the parameters of lu, mu, tu, and Tu denote the length, mass, time, and temperature units in the current simulation.

Figure 7 shows nondimensional velocity on the centerline and nondimensional slip velocity on the upper walls, in both slip and transition regimes. As indicated in Fig. 7a, the nondimensional velocity at the centerline of nanochannel increases along the channel length, and flow with lower Knudsen number leads to a higher nondimensional velocity in the slip regime. Because of the shrinkage in the cross section of the nanochannel at $X^* = 0.5$, the velocity is more substantial past this point, and the velocity falls at $X^* = 0.5$. Figure 7b shows the reduction in nondimensional velocity in the transition regime before contraction. This behavior is more apparent for high Knudsen numbers. Due to the decrease in the cross-sectional area at $X^* = 0.5$, the velocity increases from the channel inlet up to $X^* = 0.5$ and drops afterward. Similar to the slip regime, the flow with a higher Knudsen number leads to lower central velocity in the transition regime. In both regimes, the stream with smaller Knudsen number has greater Reynolds and Mach numbers, using the equation of $\mathrm{Kn} = \sqrt{\frac{\gamma\pi}{2}}\frac{\mathrm{Ma}}{\mathrm{Re}}$, and results in higher velocity, based on $\mathrm{Ma} = \frac{u}{c_s}$. The nondimensional velocity values in the transition regime are less than those in the slip regime. Because the Reynolds number in the transition regime is lower than that of slip one. Figure 7c, d indicates downward and upward trends of the slippage velocity on the upper boundary before and after contraction, respectively. In both figures, flows with smaller Knudsen numbers correspond to higher slip velocities. For each outlet Knudsen number, the slip velocities past the channel contraction are higher than those before the decrease. Figure 7e, f present slippage velocities for the upper boundary in the transition regime before and after contraction, respectively. It is demonstrated in Fig. 7e that the slippage velocity is decreasing before the contraction, but is initially reducing, then increasing and finally again decreasing in Fig. 7f. Nevertheless, the influence of Knudsen number on the slip velocities of flow in the transition regime, where the slip velocities are more than that in the slip regime, is worth noting. It is shown that flow with more significant

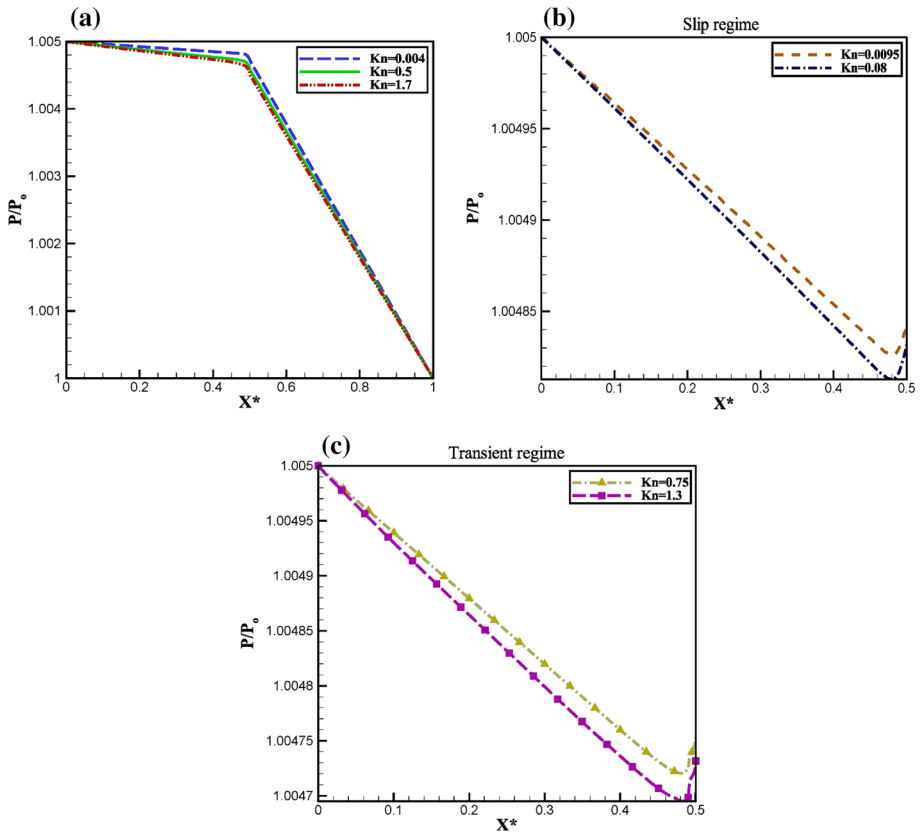

Fig. 5 Nondimensional pressures on the **a** centerline, the middle of the bottom vertical wall of nanochannel in **b** slip, and **c** transition regime at various outlet Knudsen numbers

Knudsen numbers leads to higher slip velocities. This dependency indicates that the impact of Knudsen number is more than that of the Reynolds number on nanochannel slippage velocities in the transition regime. Figure 8a shows the velocity contour in the slip regime, $\mathrm{Kn}_o = 0.0095$. The velocity increases from the inlet of the nanochannel toward the outlet. Past $X^* = 0.5$, the velocity becomes higher than its values before contraction attributable to a reduction in the cross-sectional area of nanochannel. Figure 8b shows the velocity contour in the transition regime. The velocities, in this case, are less than those observed in the slip regime, Fig. 8a. The Reynolds number in the slip regime is higher compared to the transition regime.

In Fig. 9, $C_f \cdot \mathrm{Re}$ values of the contraction nanochannel are shown. Bakhshan and Omidvar [56] offered the following equation for a dependency of $C_f \cdot \mathrm{Re}$ to Knudsen number:

$$C_f \cdot \mathrm{Re} = 3.113 + \frac{2.915}{1 + 2\mathrm{Kn}} + 0.641\exp\left(\frac{3.203}{1 + 2\mathrm{Kn}}\right) \tag{60}$$

Figure 9a shows $C_f \cdot \mathrm{Re}$ values in the slip regime along the channel length based on different Knudsen numbers. It is observed that $C_f \cdot \mathrm{Re}$ values are lower past the contraction in comparison with before the contraction. The reason is related to the growth in Knudsen number from the inlet side of nanochannel toward the outlet side which results in a decrease

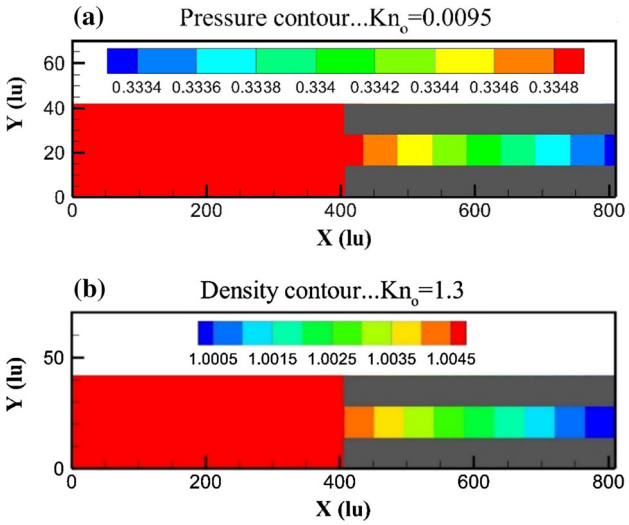

Fig. 6 Pressure and density contours based on different outlet Knudsen numbers in **a** slip and **b** transition regime

in $C_f \cdot \mathrm{Re}$ values. It is also shown that $C_f \cdot \mathrm{Re}$ amounts are more substantial for smaller Knudsen numbers that emphasize the consistency of the results with Eq. 60. Figure 9b shows a similar decreasing trend in $C_f \cdot \mathrm{Re}$ values in the transitional regime based on various outlet Knudsen numbers. Due to the higher Knudsen numbers in the transitional regime, however, $C_f \cdot \mathrm{Re}$ quantities in this regime are smaller than those for the slip regime. But the same trend and dependency on Knudsen numbers can be observed.

In Fig. 10a, the effective viscosity in the transition regime based on the outlet Knudsen number is shown. According to this figure, the flow with a more outlet Knudsen number experiences a higher value of effective viscosity. In this subsection, the effective viscosity in the transition regime is presented by $\mu_e = \frac{\mu_0}{(1+a\mathrm{Kn})} = \frac{a_0 \rho \bar{c} \lambda}{(1+a\mathrm{Kn})}$. Also, the flow with a higher Knudsen number has a higher value of density. Therefore, the effect of density on the μ_e is more significant than the Knudsen number. Also, Fig. 10a has a linear downward trend that shows the inverse correlation between the effective viscosity and Knudsen number and approves the abovementioned equation. Figure 10b shows the absolute value of shear stress obtained by $\tau = \mu_e \frac{\mathrm{d}u}{\mathrm{d}y}$ in the nanochannel before the contraction for different outlet Knudsen numbers. It is shown that a more outlet Knudsen number leads to higher shear stress. This behavior is due to the flow with high effective viscosity and the absolute value of the velocity gradient across the lateral direction of the nanochannel. Also, it is shown in Fig. 10b that the shear stress initially boosts and then decreases.

Figure 11 shows the streamlines at various outlet Knudsen numbers for the pressure ratio of 1.005. Also, the role of the rarefaction parameter on vortex creation in the nanochannel is observed. By fixed pressure ratio and *Kn* number growing, the *Re* number inclines to be smaller owing to vortices disappearance. While the rarefied gas flow starts to enter into the contraction section, it carries the less momentum (by observing Fig. 3a, d). Owing to this momentum, the flow moderately transfers to downstream of the intersection and generates a low-pressure district at the corner. On account of this low-pressure region, a part of the flow twists around and fills that region. This commences the undesirable pressure region. The adverse pressure gradient causes flow separation and leads to vortex creation. However, there

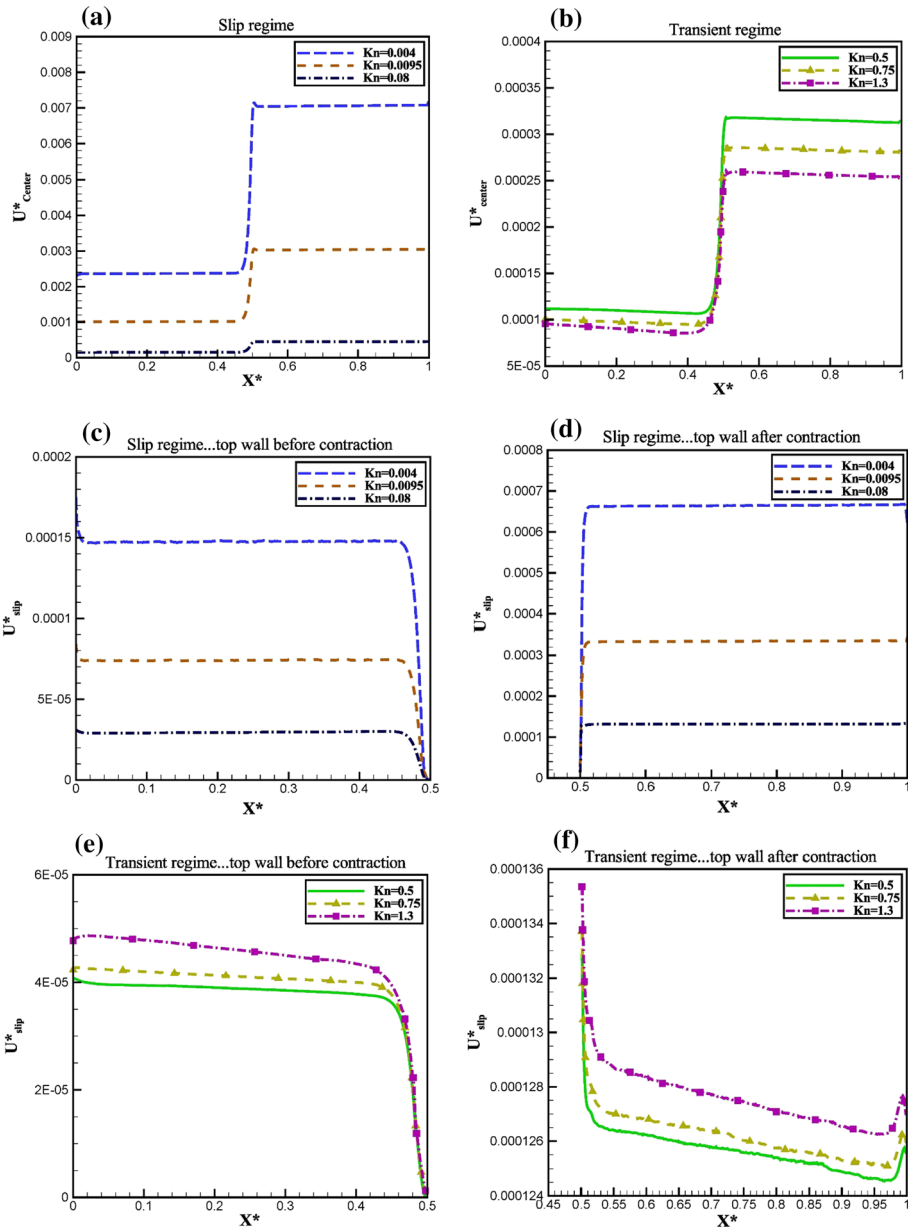

Fig. 7 Nondimensional velocities at the centerline and slip velocities in the slip and transition regimes based on the different outlet Knudsen numbers

is no flow separation in the case of an adverse pressure gradient at Kn= 1.7. This is attributable to the little momentums and their widespread diffusion, which is one of the characteristics of high Knudsen number. Therefore, the flow has oriented to the corner, and no separation is noticed. Both momentum and rarefaction perform essential roles in flow separation creation. The rarefaction effects are in two ways: diffusion and slippage on the wall. The slippage on the

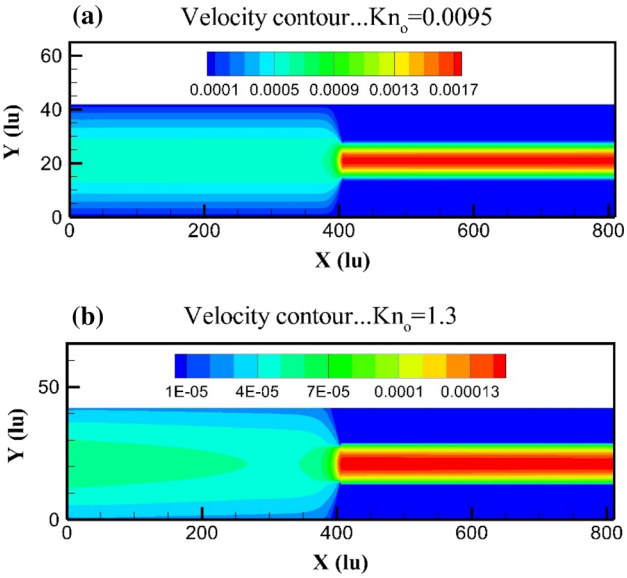

Fig. 8 Velocity contours in the **a** slip and **b** transition regimes based on various outlet Knudsen numbers

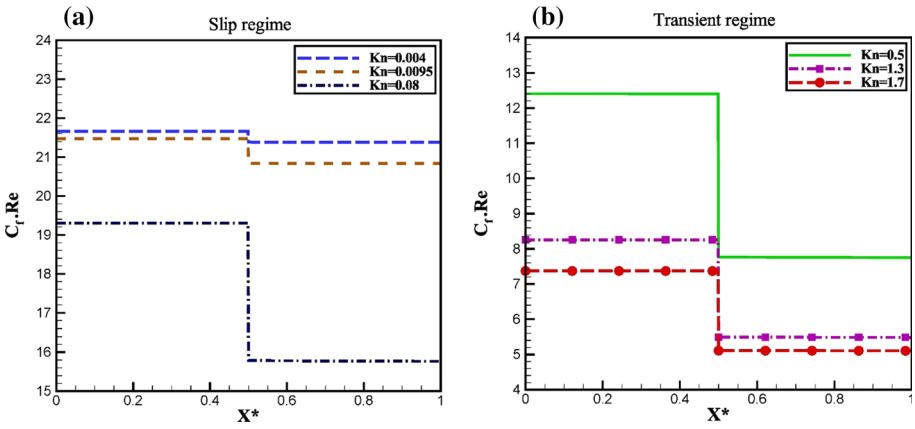

Fig. 9 $C_f.Re$ values in the **a** slip and **b** transitional regimes at different outlet Knudsen numbers

wall rises both the mass flow rate and, eventually, momentum. Therefore, the slippage helps flow separation even though the diffusion restrains the separation location. It is possible to find that the most massive vortex in size corresponds to small Knudsen numbers, i.e., slip velocity, and the vortex size decreases by the decrease in Knudsen numbers. By moving toward the transition regime, vortices disappear at high Knudsen numbers (such as Kn= 1.7).

Figure 12 shows the impact of shrinkage coefficient (α) on the pressure parameters, centerline velocity, and slippage velocity on the wall before and after the contraction in the nanochannel based on the outlet Knudsen number. The outlet Knudsen number and the outlet pressure exist equal to 1.5 and 1.005, respectively, and are constant for both transition and slip regime. It is depicted in Fig. 12a that the flow with the higher contraction coefficient, $\alpha = 7$, corresponds to a higher nondimensional pressure compared to the stream with the

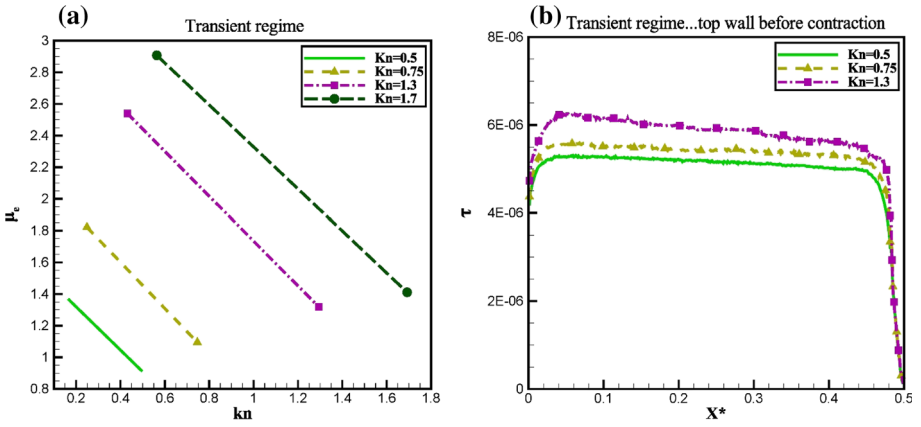

Fig. 10 **a** The variation of the effective viscosity versus the Knudsen number and **b** the change of shear stress with respect of the longitudinal of nanochannel in the transition regime based on different outlet Knudsen numbers

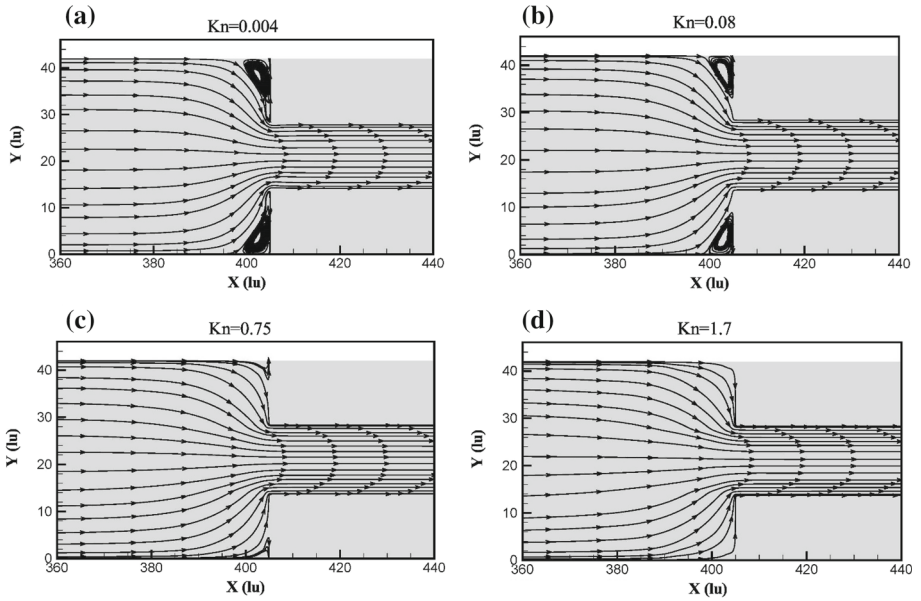

Fig. 11 The streamlines presentation and vortex creation at different outlet Knudsen numbers

shrinkage coefficient of $\alpha = 3$. Based on $\mathrm{Kn}_{\mathrm{in}} \cdot H_{\mathrm{in}} \cdot P_{\mathrm{in}} = \mathrm{Kn}(x) \cdot H(x) \cdot P(x)$ and by setting equal values to the local and outlet parameters, the inlet Knudsen number is derived as:

$$\mathrm{Kn}_{\mathrm{in}} = \frac{\mathrm{Kn}_{\mathrm{out}} \cdot H_{\mathrm{out}} \cdot P_{\mathrm{out}}}{H_{\mathrm{in}} \cdot P_{\mathrm{in}}} \rightarrow \mathrm{Kn}_{\mathrm{in}} = \frac{\mathrm{Kn}_{\mathrm{out}}}{\alpha \cdot \Pi} \tag{61}$$

Because $\mathrm{Kn}_{\mathrm{out}}$ and Π are constant, and due to the increase in the shrinkage coefficient (α), the inlet Knudsen number is smaller for the flow with a higher shrinkage coefficient (α) and the pressure. Accordingly, nondimensional pressure tends to be higher. Figures 12b, c, d show the nondimensional velocity at the centerline and upper wall in the transitional regime. It is found in all three subplots that an increase in the shrinkage coefficient, pressure

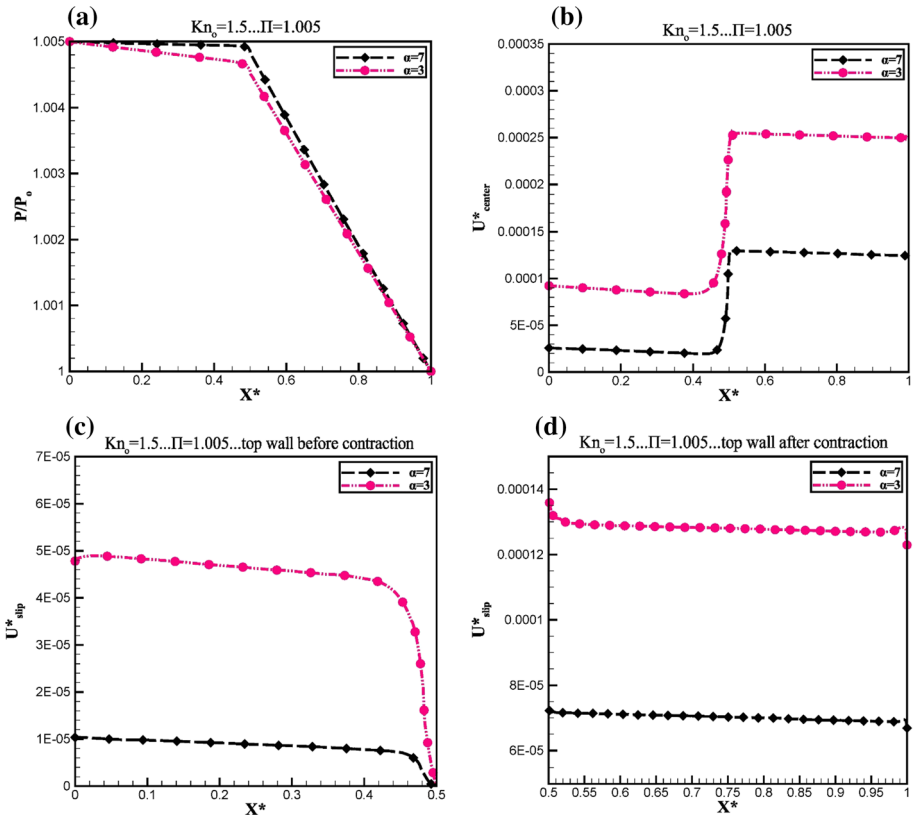

Fig. 12 The effect of shrinkage coefficient on the pressure and velocities (slip and center) for outlet Knudsen number of 1.5 at $\Pi = 1.005$

increase, and likely result in a decrease in nondimensional velocities. Figure 13 illustrates the impact of shrinkage coefficient (α) on the effective viscosity, shear stress, and $C_f \cdot \mathrm{Re}$ values in the nanochannel based on the outlet Knudsen number. Figure 13a presents the effective viscosity versus Knudsen number in the transitional regime. According to this phenomenon, the inlet Knudsen number is smaller for the flow with a higher shrinkage coefficient (α), using $\mu_e = \frac{\mu_0}{(1+a\mathrm{Kn})} = \frac{a_0 \rho \bar{c} \lambda}{(1+a\mathrm{Kn})}$. In this relation, despite the reduction of the denominator, the numerator reduces at a higher rate than the denominators. As a result, the flow with higher α corresponds to a lower effective viscosity. Furthermore, in both regimes, a linear downward trend of viscosity for increasing Knudsen numbers is observed. Figure 13b shows the absolute value of the shear stress on the wall of the nanochannel upstream of the contraction. The shear stress is less for the flow with the higher shrinkage coefficient, $\alpha = 7$, in comparison to the case with the shrinkage coefficient of $\alpha = 3$, which is originated from lower viscosity contribution. Figure 13c shows the variation of $C_f \cdot \mathrm{Re}$ values along the nanochannel for both shrinkage coefficients. Because of the constant outlet Knudsen number and low range of changes in the Knudsen number, they coincide downstream of the contraction in the nanochannel. Due to the small inlet Knudsen number for the flow inside the nanochannel with a shrinkage coefficient of $\alpha = 7$, and the inverse relation between Knudsen number and $C_f \cdot \mathrm{Re}$ values, the stream with more significant shrinkage coefficient corresponds to higher $C_f \cdot \mathrm{Re}$ values.

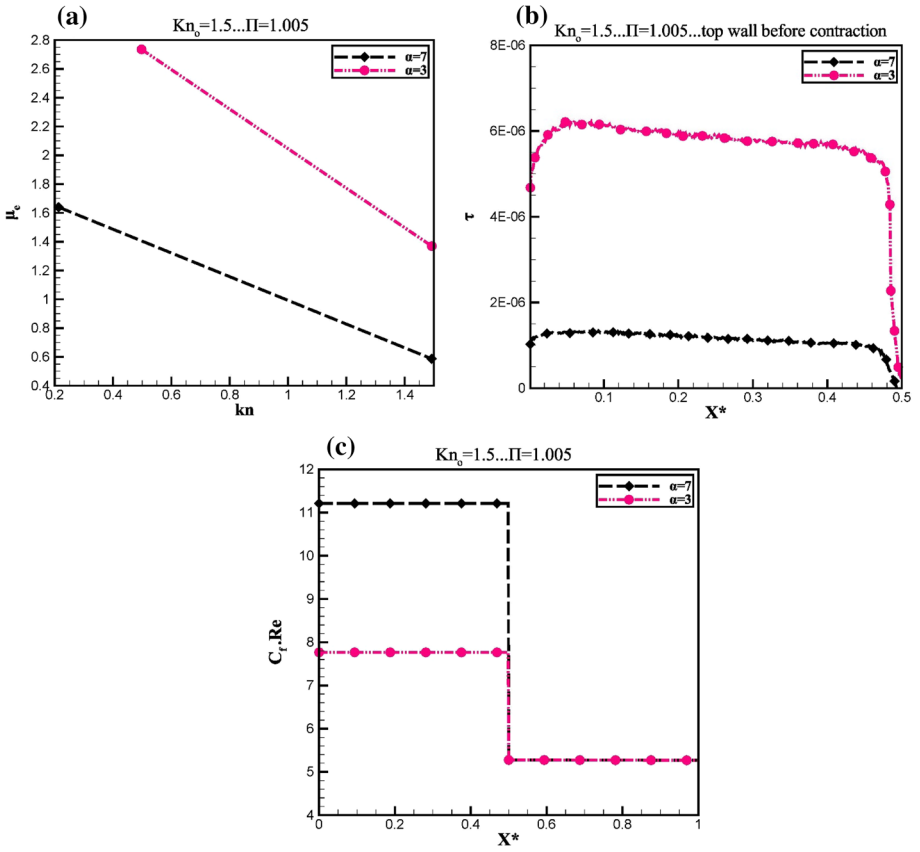

Fig. 13 The effect of shrinkage coefficient on the **a** effective viscosity, **b** shear stress, and **c** $C_f \cdot \mathrm{Re}$ values at $\mathrm{Kn}_o = 1.5$

In recent years, researchers have provided mass flow rate based on the mean Knudsen number, an average of inlet and outlet Knudsen number, and mean rarefaction parameter. Gavasane et al. [16] calculated the mass flow rate based on the inlet Knudsen number in a microchannel with a backward-facing microstep. They introduced the mass flow rate reductions by raising the inlet Knudsen number. Furthermore, Wu and Tseng [57] obtained the plot of the normalized mass flow rate base on the pressure ratio in a micro-nozzle. They reported an inverse relation to these two parameters. However, Wang and Li [58] concluded the direct correlation between mass flow rate and pressure drop for orifice flow. Gavasane et al. [16] reported the following expression for the mean rarefaction parameter based on the mean Knudsen number, which shows the inverse relationship between these two parameters.

$$\delta_m = \frac{\sqrt{\pi}}{2} \frac{1}{\mathrm{Kn}_m} \tag{62}$$

They also reported the mean rarefaction parameter based on the mean pressure(P_m), height (h), viscosity (μ), and velocity (V_0) as follows:

$$\delta_m = \frac{h P_m}{\mu V_0} \tag{63}$$

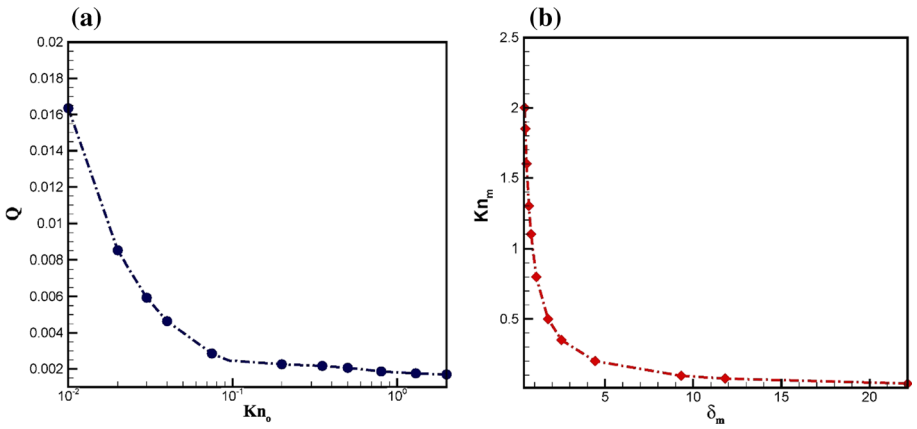

Fig. 14 **a** Mass flow rate based on different outlet Knudsen numbers at $\Pi = 1.005$ and **b** expression of mean Knudsen number with the mean rarefaction parameter

where mean pressure is reported as $P_m = \frac{P_{\text{in}}+P_{\text{out}}}{2}$. The mass flow rate in this simulation is considered as $\dot{Q} = \int_0^H \rho(y) \cdot u(y) \cdot \mathrm{d}y$. Figure 14a shows the dependency of the mass flow rate (in the lattice unit, $\frac{\text{mu}}{\text{tu}}$) on the outlet Knudsen number. According to the previous studies [14, 16, 55, 58], a downward trend is expected. Also, by growing the outlet Knudsen number, for the flow trend in the range $0.5 < \text{Kn} < 2$, the slope of the plot is decreased while it is significant in the slip regime. Figure 14b shows the variation of mean Knudsen number with the mean rarefaction parameter and shows a downward trend.

4 Conclusions

In the present work, the rarefied gas flow in contracting nanochannel is simulated by the TRT solver of a mesoscopic computational fluid dynamic approach. The symmetric relaxation time based on the Bosanquet-type effective viscosity for transition regime is applied. The main results of numerical simulation are shown as follows:

- The nondimensional pressure profile for the center of the bottom vertical wall versus the X^* is parabolic due to favorable pressure gradient before the contraction and presence of vortexes at the vicinity of the bent region.
- The flow with lower Knudsen number has a higher slip velocity, but an opposite relationship is noticed between the two mentioned parameters in the transition regime owing to rarefaction influence.
- By increasing the Knudsen number, the vortices become smaller in the contraction nanochannel and tend to vanish at higher Knudsen numbers.
- Both momentum and rarefaction perform essential roles in the separation phenomena.
- Shrinkage coefficient (α) growth leads to a rise in the nondimensional pressure and $C_f \cdot \text{Re}$ values, but a decrease in the values of nondimensional velocities, the absolute value of shear stress before the contraction, and the effective viscosity is found.
- The mass flow rate has an inverse relationship to the outlet Knudsen number.

Acknowledgements The English language review of this paper is performed by Dr. Seama Koohi-Fayegh (UOIT).

References

1. R. Arabjamaloei, D.W. Ruth, J. Nat. Gas Sci. Eng. (2016). https://doi.org/10.1016/j.jngse.2016.03.056
2. P.L.L. Walls, B. Abedian, Int. J. Eng. Sci. (2014). https://doi.org/10.1016/j.ijengsci.2014.02.002
3. Y. Qi, Y. Che, S. Pan, H. Zhang, Int. J. Heat Mass Transf. (2019). https://doi.org/10.1016/j.ijheatmasstransfer.2019.03.154
4. J. Sun, Y. He, W. Tao, X. Yin, H. Wang, Int. J. Numer Methods Eng. (2012). https://doi.org/10.1002/nme.3229
5. E.K. Ahangar, M.B. Ayani, J.A. Esfahani, K.C. Kim, Vacuum (2020). https://doi.org/10.1016/j.vacuum.2019.109104
6. Q. Lv, X. Liu, E. Wang, S. Wang, Phys. Rev. E (2013). https://doi.org/10.1103/PhysRevE.88.013007
7. E. B. Arkilic, M.A. Schmidt, K.S. Breuer. (1997). IEEE. https://doi.org/10.1109/84.585795
8. M.T. Ho, J. Li, W. Su, L. Wu, M.K. Borg, Z. Li, Y. Zhang, J. Fluid Mech. (2020). https://doi.org/10.1017/jfm.2020.585
9. M. Zhong, S. Zou, D. Pan, C. Zhuo, C. Zhong, Physics of Fluids (2020). https://doi.org/10.1063/5.0021332
10. C. Baranger, Y. Dauvois, G. Marois, J. Mathé, J. Mathiaud, L. Mieussens, European Journal of Mechanics - B/Fluids. (2020). https://doi.org/10.1016/j.euromechflu.2019.11.006
11. L. Wu, H. Struchtrup, J. Fluid Mech. (2017). https://doi.org/10.1017/jfm.2017.326
12. S. Taguchi, K. Saito, S. Takata, J. Fluid Mech. (2019). https://doi.org/10.1017/jfm.2018.946
13. V. Varade, A. Agrawal, A.M. Pradeep, J. Fluid Mech. (2014). https://doi.org/10.1017/jfm.2013.615
14. J.G. Meolans, T. Veltzke, M.T. Ho, J. Thöming, I. Graur, Microfluid. Nanofluid. (2014). https://doi.org/10.1007/s10404-014-1445-4
15. A. Taassob, R. Kamali, A. Bordbar, Vacuum (2018). https://doi.org/10.1016/j.vacuum.2018.02.021
16. A. Gavasane, A. Agrawal, U. Bhandarkar, Vacuum (2019). https://doi.org/10.1016/j.vacuum.2018.06.014
17. O. Sazhin, Microfluidics and Nanofluidics (2020). https://doi.org/10.1007/s10404-020-02384-w
18. D. Nabapure, K.R.C. Murthy, Acta Astronaut. (2020). https://doi.org/10.1016/j.actaastro.2020.08.030
19. E.K. Ahangar, S. Fallah-Kharmiani, S.D. Khakhian, L.P. Wang, Phys. Fluids (2020). https://doi.org/10.1063/5.0008325
20. A. Zarei, A. Karimipour, A.H.M. Isfahani, Z. Tian, Physica A (2019). https://doi.org/10.1016/j.physa.2019.122453
21. M. Mozaffari, A. D'Orazio, A. Karimipour, A. Abdollahi, M.R. Safaei, Int. J. Numer. Meth. Heat Fluid Flow (2019). https://doi.org/10.1108/HFF-12-2018-0821
22. S. Aghakhani, A.H. Pordanjani, A. Karimipour, A. Abdollahi, M. Afrand, Comput. Fluids (2018). https://doi.org/10.1016/j.compfluid.2018.09.012
23. A.A. Balootaki, A. Karimipour, D. Toghraie, Physica A (2018). https://doi.org/10.1016/j.physa.2018.05.141
24. E.K. Ahangar, M. Izanlu, S.D. Khakhian, A.A. Mohamad, Q.V. Bach, J. Therm. Anal. Calorim. (2020). https://doi.org/10.1007/s10973-020-10129-8
25. A. D'Orazio, A. Karimipour, Int. J. Heat Mass Transf. (2019). https://doi.org/10.1016/j.ijheatmasstransfer.2019.03.029
26. H. Nazarafkan, B. Mehmandoust, D. Toghraie, A. Karimipour, Int. J. Numer. Methods Heat Fluid Flow (2019). https://doi.org/10.1108/HFF-11-2018-0686
27. Q. Nguyen, M.J. Ghahderijani, M. Bahrami, E.K. Ahangar, A. D'Orazio, Q.V. Bach, A. Karimipour, Math. Methods. Appl. Sci. (2020). https://doi.org/10.1002/mma.6513
28. A. Karimipour, A. D'Orazio, M. Goodarzi, Physica A (2018). https://doi.org/10.1016/j.physa.2018.06.031
29. J.M. Tucny, D. Vidal, S. Leclaire, F. Bertrand, Int. J. Mod. Phys. C (2020). https://doi.org/10.1142/S0129183120500709
30. M. Timokhin, M. Tikhonov. (2019). https://doi.org/10.1063/1.5119653
31. X. Niu, S. Hyodo, K. Suga, H. Yamaguchi, Comput. Fluids (2009). https://doi.org/10.1016/j.compfluid.2009.02.003
32. H. Wang, H. Zhao, Z. Guo, Y. He, C. Zheng, J. Comput. Phys. (2013). https://doi.org/10.1016/j.jcp.2012.12.032
33. Q. Li, Y.L. He, G.H. Tang, W.Q. Tao, Microfluid. Nanofluid. (2011). https://doi.org/10.1007/s10404-010-0693-1
34. A. Kakouei, A. Vatani, M. Rasaei, B.S. Sola, H. Moqtaderi. (2017). https://doi.org/10.1016/j.jngse.2017.06.018
35. M. Ho, J.G. Pérez, M. Reggio, J. Trépanier. (2019). https://doi.org/10.1016/j.pce.2019.02.014

36. J. Wang, Q. Kang, Y. Wang, R. Pawar, S.S. Rahman, Fuel (2017). https://doi.org/10.1016/j.fuel.2017.05.080
37. J. Wang, L. Chen, Q. Kang, S.S. Rahman, Int. J. Heat Mass Transf. (2016). https://doi.org/10.1016/j.ijheatmasstransfer.2015.12.009
38. A. Norouzi, J. Abolfazli, J. Stat. Phys. (2015). https://doi.org/10.1007/s10955-015-1420-9
39. E.K. Ahangar, M.B. Ayani, J.A. Esfahani, Int. J. Mech. Sci. (2019). https://doi.org/10.1016/j.ijmecsci.2019.05.025
40. I. Ginzburg, Adv. Water Resour. (2005). https://doi.org/10.1016/j.advwatres.2005.03.004
41. S. Chapman, T.G. Cowling, *The Mathematical Theory of Non-uniform Gases*, 3rd edn. (Cambridge University Press, Cambridge, 1970)
42. A. Beskok, G.E. Karniadakis, Microscale Thermophys. Eng. (2010). https://doi.org/10.1080/10893959199864
43. V.K. Michalis, A.N. Kalarakis, E.D. Skouras, V.N. Burganos, D.Á. Straight, Microfluid. Nanofluid. (2010). https://doi.org/10.1007/s10404-010-0606-3
44. S. Yuhong, W.K. Chan, S. Yuhong, W.K. Chan, J. Vac. Sci. Technol., A (2004). https://doi.org/10.1116/1.1647599
45. X. Liu, Z. Guo, *Comput* (Appl, Math, 2013). https://doi.org/10.1016/j.camwa.2011.01.035
46. X.Z. Li, J.C. Fan, H. Yu, Y.B. Zhu, H.A. Wu. (2018). Int J Heat Mass Transf. https://doi.org/10.1016/j.ijheatmasstransfer.2018.02.066
47. Z. Guo, C. Zheng, B. Shi, Phys. Rev. E (2008). https://doi.org/10.1103/PhysRevE.77.036707
48. C. Cercignani, *Mathematical Methods in Kinetic Theory* (Springer, New York, 1988)
49. N.G. Hadjiconstantinou, Phys. Fluids (2003). https://doi.org/10.1063/1.1587155
50. Y.T. Hsia, G.A. Domoto, J. Lubrication Tech. (1983). https://doi.org/10.1115/1.3254526
51. S.K. Loyalka, Phys. Fluids (1971). https://doi.org/10.1063/1.1693380
52. S.K. Loyalka, N. Petrellis, T.S. Storvick. Phys. Fluids (1975). https://doi.org/10.1063/1.861293
53. A.A. Mohamad, *Lattice Boltzmann method*, 2nd edn. (Springer, London, 2011)
54. N. Mosavat, B. Hasanidarabadi, P. Pourafshary, J. Petrol. Sci. Eng. (2019). https://doi.org/10.1016/j.petrol.2019.02.029
55. Z. Guo, C. Shu, *Lattice Boltzmann method and its applications in engineering* (World Scientific Publishing, Singapore, 2013)
56. Y. Bakhshan, A. Omidvar, Physica A (2015). https://doi.org/10.1016/j.physa.2015.08.012
57. J. Wu, K. Tseng, Comput. Fluids (2001). https://doi.org/10.1016/S0045-7930(00)00029-3
58. M. Wang, Z. Li, Int. J. Heat Fluid Flow (2004). https://doi.org/10.1016/j.ijheatfluidflow.2004.02.024